Hindawi
Journal of Sensors
Volume 2021, Article ID 8301359, 16 pages
https://doi.org/10.1155/2021/8301359

Research Article

Speed Sensor-Less Control System of Surface-Mounted Permanent Magnet Synchronous Motor Based on Adaptive Feedback Gain Supertwisting Sliding Mode Observer

Lei Zhang, Jing Bai, and Jing Wu

College of Electrical and Information Engineering Beihua University, Ji Lin 132013, China

Correspondence should be addressed to Jing Bai; jlbyj@163.com

Received 24 July 2021; Revised 7 September 2021; Accepted 19 September 2021; Published 20 October 2021

Academic Editor: Chun-xi Yang

Aiming at the problems of severe chattering and difficulty in low-speed operation of the surface-mounted permanent magnet synchronous motor (SPMSM) sensor-less speed control system based on the traditional sliding mode observer (SMO), this paper proposes a sensor-less control strategy of supertwisting sliding mode observer based on adaptive feedback gain (AFG-STA-SMO). This strategy combines the supertwisting algorithm (STA) with the equivalent feedback principle and designs an adaptive law to compensate for the rotor position error by adjusting the feedback gain coefficient online. Secondly, considering the ripple component in the back electromotive force (back-EMF), the Kalman filter gets a smoother back-EMF signal, further improving the rotor position estimation accuracy. The stability of the system is proved by using the Lyapunov function. Finally, the feasibility and effectiveness of the proposed control strategy are verified by MATLAB/Simulink simulation.

1. Introduction

Surface-mounted permanent magnet synchronous motor has a small size, high power density, high efficiency, low rotor loss, and solid environmental adaptability [1–4]. It is widely used in the wind power generation system and industrial transmission field. In order to realize high-performance control of permanent magnet synchronous motor, it is necessary to install speed and position sensors such as a photoelectric encoder to get accurate rotor position and speed information. However, installing a photoelectric encoder will increase the system's cost and require a high operating environment [5]. As a result, various sensor-less techniques have been developed to estimate rotor position and speed over the past few decades.

At present, speed sensor-less control algorithms are mainly divided into two categories: the high-frequency signal injection method, which depends on the motor's salient spatial characteristics. Accurate rotor position information can be obtained at all speeds, including zero speed, but it is only applicable to the built-in motor with much noise. The second type uses the motor speed parameters (such as the back-EMF) in the motor fundamental excitation mathematical model to estimate the rotor position and speed, which has significant dynamic performance but is only suitable for the operation range of medium and high-speed. The commonly used fundamental back-EMF observation algorithms include SMO [6–9], model reference adaptive [10–11], and extended Kalman filter [12]. SMO has been widely studied because of its simple implementation, insensitivity to parameter changes, and external interference [13]. However, the chattering caused by the sign switching function is an inevitable problem in SMO. Therefore, the low-pass filter (LPF) was introduced to filter the back-EMF. Since the traditional LPF cut-off frequency is fixed, the back-EMF's ripple component cannot be eliminated, seriously affecting the rotor position's estimation accuracy [14]. In literature [15], an adaptive filter is proposed to filter out the sliding mode noise, but the causes of the system's phase delay to a certain extent. The literature [16–18] proposed an SMO based on the supertwisting algorithm to observe back-EMF to solve this problem. This method can effectively suppress the chattering phenomenon caused by the switching function, and a good control effect can be

obtained in the medium and high-speed range. However, with the decrease of motor speed, the back-EMF gradually decreases, and the observation accuracy also decreases. In order to improve the rotor estimation when the motor runs at low speed, an SMO is based on equivalent feedback proposed in the literature [19]. The observer can feed back on the estimated back-EMF to the stator current observation and calculation to achieve the motor's low-speed operation. However, the feedback gain coefficient is only selected according to the speed, so the algorithm lacks adaptability. Based on the equivalent feedback sliding mode observer, a feedback gain adaptive algorithm is proposed in the literature [20, 21] to realize the rotor angle compensation at different speeds. However, this method still needs to introduce an LPF and compensate for the rotor position delay, which increases the complexity of the system.

In this paper, an STA-SMO with adaptive feedback gain was proposed by combining the equivalent feedback principle with the supertwisting algorithm. The observer feeds back on the estimated back-EMF to the stator current observation and calculation and designs an adaptive law to realize rotor angle compensation at different speeds, which improves the observer's low-speed performance and simplifies the selection of sliding mode gain. Simultaneously, the Kalman filter is used to filter out the ripple component in the back-EMF and further improve the sensor-less control precision; the Lyapunov function analyzes the system's stability.

2. Design of SMO

2.1. Mathematical Model of SPMSM. The mathematical model of surface-mounted PMSM, theα-βstationary coordinate system, is [22]

$$\begin{bmatrix} U\alpha \\ U\beta \end{bmatrix} = \begin{bmatrix} R + \dfrac{\mathrm{d}}{dt}L & 0 \\ 0 & R + \dfrac{\mathrm{d}}{dt}L \end{bmatrix} \begin{bmatrix} i\alpha \\ i\beta \end{bmatrix} + \begin{bmatrix} E\alpha \\ E\beta \end{bmatrix}, \tag{1}$$

where $U\alpha\beta$, $i\alpha\beta$, $E\alpha\beta$, R, and L are α-β axis voltages, α-β axis currents, α-β axis back-EMFs, stator resistance, and stator inductance, respectively. And $E\alpha\beta$ satisfies

$$\begin{bmatrix} E\alpha \\ E\beta \end{bmatrix} = (\omega e \psi f) \begin{bmatrix} -\sin\theta e \\ \cos\theta e \end{bmatrix}, \tag{2}$$

where ψf is the flux linkage, θe is the rotor position angle, and ωe is the rotational speed.

The derivative of equation (2) is obtained:

$$\frac{d}{dt}\begin{bmatrix} E\alpha \\ E\beta \end{bmatrix} = \omega e \begin{bmatrix} -\psi f \omega e \cos\theta e \\ -\psi f \omega e \sin\theta e \end{bmatrix} = \omega e \begin{bmatrix} -E\beta \\ E\alpha \end{bmatrix}. \tag{3}$$

As shown in equation (3), the back-EMF contains the rotor position and speed information.

2.2. Traditional SMO. In order to obtain the back-EMF, equation (1) is rewritten as follows:

$$\frac{d}{dt}\begin{bmatrix} i\alpha \\ i\beta \end{bmatrix} = -\frac{R}{L}\begin{bmatrix} i\alpha \\ i\beta \end{bmatrix} + \frac{1}{L}\begin{bmatrix} U\alpha \\ U\beta \end{bmatrix} - \frac{1}{L}\begin{bmatrix} E\alpha \\ E\beta \end{bmatrix}. \tag{4}$$

According to equation (4), the traditional SMO can be designed as

$$\frac{d}{dt}\begin{bmatrix} \hat{i}\alpha \\ \hat{i}\beta \end{bmatrix} = -\frac{R}{L}\begin{bmatrix} \hat{i}\alpha \\ \hat{i}\beta \end{bmatrix} + \frac{1}{L}\begin{bmatrix} U\alpha \\ U\beta \end{bmatrix} - \frac{1}{Ls}\begin{bmatrix} v\alpha \\ v\beta \end{bmatrix}, \tag{5}$$

where $\hat{i}\alpha\beta$ is the observed value of stator current, $U\alpha\beta$ is the control input of the observer, and $v\alpha\beta$ is the estimated value of the back electromotive force.

$$\begin{bmatrix} v\alpha \\ v\beta \end{bmatrix} = \begin{bmatrix} k\ \mathrm{sign}\left(\hat{i}\alpha - i\alpha\right) \\ k\ \mathrm{sign}\left(\hat{i}\beta - i\beta\right) \end{bmatrix}, \tag{6}$$

where sign () is the signum function and k is the sliding mode gain coefficient.

From equation (6), it can be seen that there is a discontinuous function sign () in the estimated back-EMF value, which makes the back-EMF contain a large number of sliding mode noise and harmonic components, so it needs to introduce a LPF to filter it. Since the phase and amplitude errors are introduced into the LPF, it must be compensated, which increases the complexity of the system.

In order to further improve the low-speed performance of speed sensor-less control, a SMO based on equivalent feedback electromotive force was proposed in literature [19], as shown in the following equation:

$$\frac{d}{dt}\begin{bmatrix} \hat{i}\alpha \\ \hat{i}\beta \end{bmatrix} = -\frac{R}{L}\begin{bmatrix} \hat{i}\alpha \\ \hat{i}\beta \end{bmatrix} + \frac{1}{L}\begin{bmatrix} U\alpha \\ U\beta \end{bmatrix} - \frac{1}{Ls}\begin{bmatrix} v\alpha + \varepsilon v\alpha\mathrm{eq} \\ v\beta + \varepsilon v\beta\mathrm{eq} \end{bmatrix}, \tag{7}$$

where ε is the feedback gain coefficient and $v\alpha\beta$eq are the equivalent feedback electromotive force values.

$$\begin{bmatrix} v\alpha\mathrm{eq} \\ v\beta\mathrm{eq} \end{bmatrix} = \begin{bmatrix} \dfrac{\omega c}{\tau s + \omega c} v\alpha \\ \dfrac{\omega c}{\tau s + \omega c} v\beta \end{bmatrix}, \tag{8}$$

where ωc is the cut-off frequency of the LPF and τ is the time constant of the LPF.

When the motor is running at low speed, the SMO based on the equivalent feedback EMF can improve the value of the equivalent feedback EMF by reasonably designing parameter ε, so as to solve the problem that the response EMF is too small and the rotor position cannot be estimated effectively, and improve the control precision of the system. However, the method still needs to introduce a low-pass filter and conduct behavior compensation.

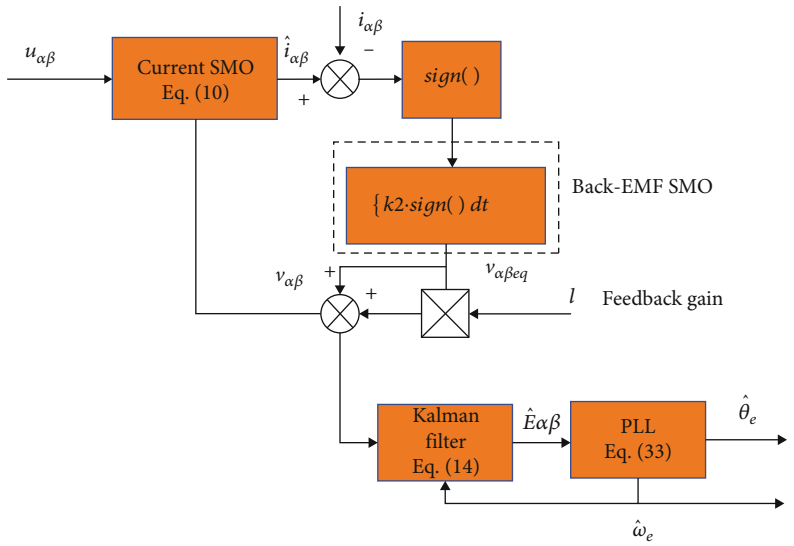

Figure 1: Block diagram of AFG-STA-SMO.

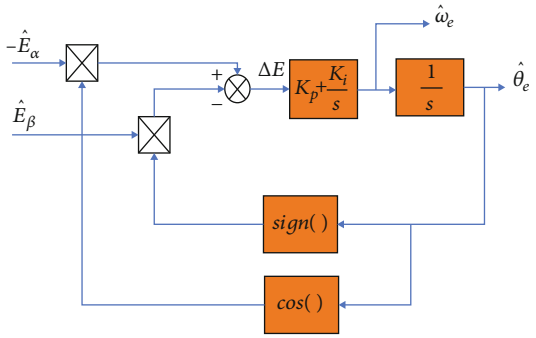

Figure 2: Schematic diagrams of PLL.

In order to retain the advantages of the equivalent feedback SMO and avoid using a LPF, a new sliding mode speed sensor-less control method was designed in literature [23]. In this method, a new state observer is designed to observe the equivalent feedback signal $v\alpha\beta$eq, thus avoiding the use of a LPF. However, the design and debugging of the state observer are complicated.

3. Design of AFG-STA-SMO

3.1. Supertwisting Algorithm. The general form of the supertwisting algorithm [17] is as follows:

$$\begin{aligned}\frac{d\tilde{x}1}{dt} &= -k1|\tilde{x}1|^{1/2}\ \text{sign}\ (\tilde{x}1) + x2 + \rho 1,\\ \frac{d\tilde{x}2}{dt} &= -k2\ \text{sign}\ (\tilde{x}1) + \rho_2,\end{aligned} \tag{9}$$

where xi, $\hat{x}i$, $\tilde{x}i$, ki, ρi, and sign () are state variables, estimation of state variables, the error between estimated and actual state variables, sliding mode gain coefficient, perturbation term, and signum function, respectively.

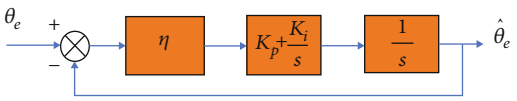

Figure 3: Equivalent schematic diagrams of PLL.

3.2. AFG-STA-SMO. Since SPMSM high-precision vector control requires accurate motor speed and rotor position information, traditional SMO has parameter perturbation and chattering. This paper combines the principle of equivalent feedback with STA-SMO, and the design is as follows:

$$\begin{cases}\dfrac{d}{dt}\begin{bmatrix}\hat{i}\alpha\\ \hat{i}\beta\end{bmatrix} = -\dfrac{R}{L}\begin{bmatrix}\hat{i}\alpha\\ \hat{i}\beta\end{bmatrix} + \dfrac{1}{L}\begin{bmatrix}U\alpha\\ U\beta\end{bmatrix} - \dfrac{1}{L}\begin{bmatrix}v\alpha + l\cdot v\alpha\text{eq}\\ v\beta + l\cdot v\beta\text{eq}\end{bmatrix} - \begin{bmatrix}k1\cdot|\tilde{i}\alpha|^{1/2}\cdot\text{sign}\ (\tilde{i}\alpha)\\ k1\cdot|\tilde{i}\beta|^{1/2}\cdot\text{sign}\ (\tilde{i}\beta)\end{bmatrix},\\ \dfrac{d}{dt}\begin{bmatrix}v\alpha\\ v\beta\end{bmatrix} = \begin{bmatrix}k2\cdot\text{sign}\ (\tilde{i}\alpha)\\ k2\cdot\text{sign}\ (\tilde{i}\beta)\end{bmatrix},\\ \begin{bmatrix}v\alpha\text{eq}\\ v\beta\text{eq}\end{bmatrix} = \begin{bmatrix}v\alpha\\ v\beta\end{bmatrix},\end{cases} \tag{10}$$

where l is the feedback gain coefficient, $\hat{i}\alpha\beta$ are the observation value of the stator currents, $U\alpha\beta$ are α-β axis voltages, $-((R/L)i\alpha) + ((1/L)U\alpha)$ and $-((R/L)i\beta) + ((1/L)U\beta)$ are regarded as the perturbation terms, $v\alpha = \int k2\cdot\text{sign}\ (\tilde{i}\alpha)dt$ and $v\beta = \int k2\cdot\text{sign}\ (\tilde{i}\beta)dt$ are the estimated value of back-EMFs, and $v\alpha$eq and $v\beta$eq are the equivalent feedback electromotive force values.

The difference between equations (4) and (10) can be obtained:

$$\frac{d}{dt}\begin{bmatrix}\tilde{i}\alpha\\ \tilde{i}\beta\end{bmatrix} = -\frac{Rs}{Ls}\begin{bmatrix}\tilde{i}\alpha\\ \tilde{i}\beta\end{bmatrix} - \frac{1}{Ls}\begin{bmatrix}\tilde{e}\alpha\\ \tilde{e}\beta\end{bmatrix} - \begin{bmatrix}k1\cdot|\tilde{i}\alpha|^{1/2}\cdot\text{sign}\ (\tilde{i}\alpha)\\ k1\cdot|\tilde{i}\beta|^{1/2}\cdot\text{sign}\ (\tilde{i}\beta)\end{bmatrix}, \tag{11}$$

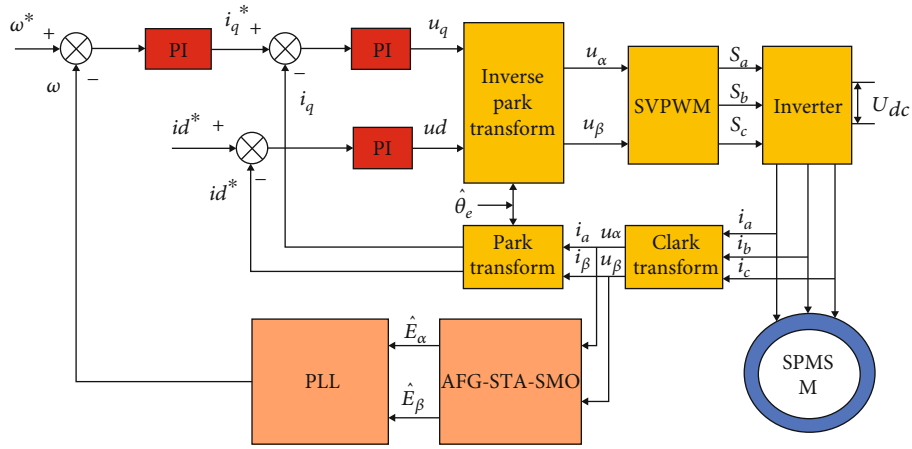

Figure 4: SPMSM speed sensor-less control block diagram of AFG-STA-SMO.

where $\tilde{i}\alpha = \hat{i}\alpha - i\alpha$, $\tilde{i}\beta = \hat{i}\beta - i\beta$, $\tilde{e}\alpha = v\alpha + lv\alpha\text{eq} - E\alpha$, and $\tilde{e}\beta = v\beta + lv\beta\text{eq} - E\beta$.

After the state variable of the observer reaches the sliding mode surface $\tilde{i}\alpha = 0$ and $\tilde{i}\beta = 0$, according to the sliding mode variable structure equivalent principle, we can get

$$\begin{bmatrix} E\alpha \\ E\beta \end{bmatrix} = \begin{bmatrix} v\alpha + lv\alpha\text{eq} \\ v\beta + lv\beta\text{eq} \end{bmatrix} = \begin{bmatrix} (1+l)\cdot \int k2 \cdot \text{sign}\left(\tilde{i}\alpha\right)dt \\ (1+l)\cdot \int k2 \cdot \text{sign}\left(\tilde{i}\beta\right)dt \end{bmatrix}. \tag{12}$$

From equation (12), the integral term $v\alpha\beta$ filters out high-frequency sliding mode noise, so introducing low-pass filters and phase compensation is avoided, and the system algorithm is simplified. It can be seen from equation (12) that the sliding mode gain $k2$ and feedback gain l are proportional to the speed. When the motor is running at high speed, the sliding-mode gain $k2$ and the feedback gain l are larger. When the motor runs at low speed, the sliding-mode gain $k2$ and the feedback gain l are smaller.

3.3. Optimization of AFG-STA-SMO. The derivative of equation (12) is obtained:

$$\begin{cases} \dfrac{d}{dt}E\alpha = -\omega e \cdot E\beta = (1+l)\cdot k2 \cdot \text{sign}\left(\tilde{i}\alpha\right), \\ \dfrac{d}{dt}E\beta = \omega e \cdot E\alpha = (1+l)\cdot k2 \cdot \text{sign}\left(\tilde{i}\beta\right). \end{cases} \tag{13}$$

Although the harmonic component is effectively filtered by integral operation, the back-EMF's observed value still contains a ripple component, which will lead to error if used to estimate the rotor position directly. Therefore, the Kalman filter is used in this paper to obtain a smoother back-EMF signal, which further improves the rotor position estimation accuracy.

Table 1: SPMSM parameters.

Parameters	Values
Stator resistance R_s	2.875 Ω
Pole-pair number	4
Magnetic flux ψ_f	0.175 Wb
D-axis induction L_d	8.5e-3H
Q-axis induction L_q	8.5e-3H
Damping factor B	0
DC bus voltage U_{dc}	310 V
Pole-pair number	4
Magnetic flux ψ_f	0.175 Wb
Rotational inertia J	0.001 kg·m^2

According to equation (13), the state equation of the Kalman filter is designed as [24]

$$\begin{bmatrix} \dfrac{d}{dt}\hat{E}\alpha \\ \dfrac{d}{dt}\hat{E}\beta \\ \dfrac{d}{dt}\hat{\omega}e \end{bmatrix} = \begin{bmatrix} -\hat{E}\beta\hat{\omega}e - \tilde{E}\alpha\lambda \\ \hat{E}\alpha\hat{\omega}e - \tilde{E}\beta\lambda \\ \hat{E}\beta\tilde{E}\alpha - \hat{E}\alpha\tilde{E}\beta \end{bmatrix}, \tag{14}$$

where λ is the adaptive gain, $\hat{\omega}e$ is the estimated rotational speed, $\hat{E}\alpha$ and $\hat{E}\beta$ are the final observed values of back-EMF, $\tilde{E}\alpha = \hat{E}\alpha - v\alpha - lv\alpha\text{eq}$, and $\tilde{E}\beta = \hat{E}\beta - v\beta - lv\beta\text{eq}$.

Considering that the adaptive gain coefficient which is too large will cause the system to be unstable and too small will cause the system to converge too slowly, so this paper designs the adaptive gain according to the actual speed of the motor as

$$\lambda = \lambda a + \kappa\omega e, \tag{15}$$

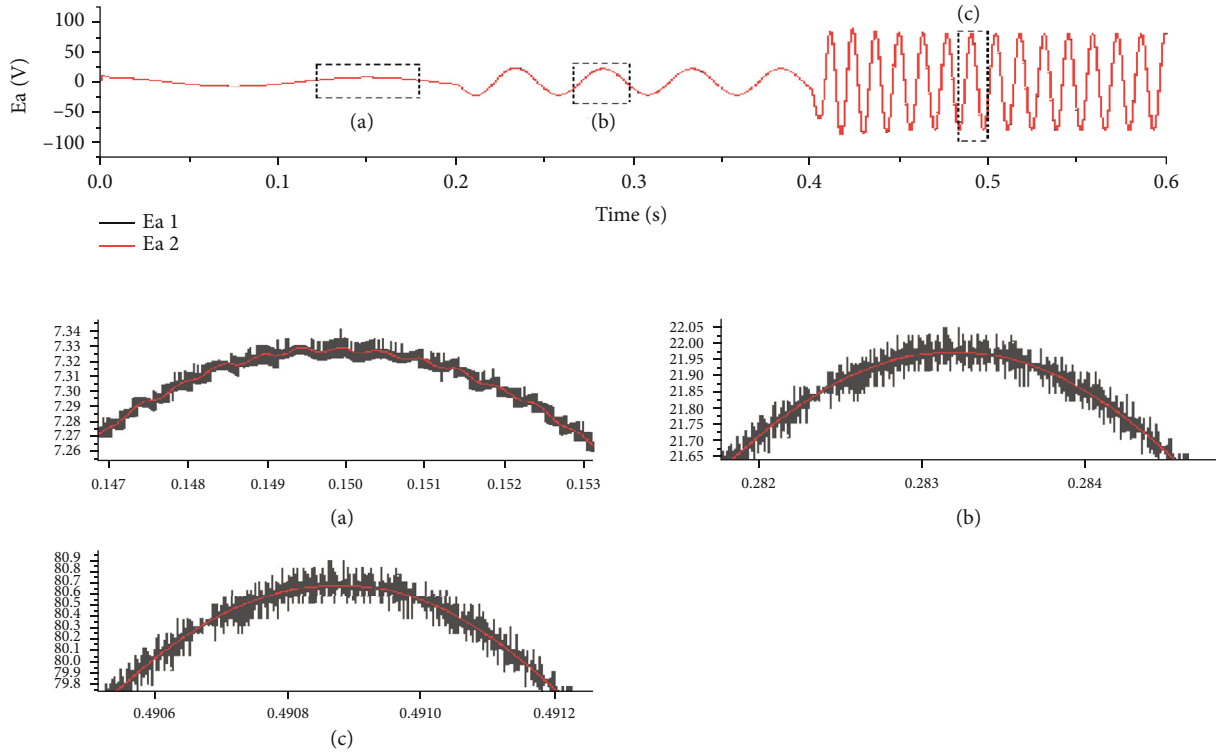

Figure 5: Back-EMF response diagram.

where λa and κ are both normal numbers and ωe represents the actual speed of the motor.

Stability analysis

$$V = \frac{1}{2}\left(\tilde{E}^2\alpha + \tilde{E}^2\beta + \tilde{\omega}^2 e\right). \tag{16}$$

where $\tilde{\omega}e = \hat{\omega}e - \omega e$.

Since the mechanical time constant is much larger than the electrical time constant, it is considered that the speed does not change within an estimation period. which can be obtained from equation (3) and equation (14):

$$\begin{bmatrix} \frac{d}{dt}\tilde{E}\alpha \\ \frac{d}{dt}\tilde{E}\beta \\ \frac{d}{dt}\tilde{\omega}e \end{bmatrix} = \begin{bmatrix} -\hat{E}\beta\tilde{\omega}e - \tilde{E}\beta\hat{\omega}e - \tilde{E}\alpha\lambda \\ \hat{E}\alpha\tilde{\omega}e + \tilde{E}\alpha\hat{\omega}e - \tilde{E}\beta\lambda \\ \hat{E}\beta\tilde{E}\alpha - \hat{E}\alpha\tilde{E}\beta \end{bmatrix}. \tag{17}$$

Substitute equation (17) into equation (16) and derive

$$\begin{aligned} \frac{d}{dt}V &= \tilde{E}\alpha\frac{d}{dt}\tilde{E}\alpha + \tilde{E}\beta\frac{d}{dt}\tilde{E}\beta + \tilde{\omega}e\frac{d}{dt}\tilde{\omega}e \\ &= -\tilde{E}\alpha\hat{E}\beta\tilde{\omega}e - \tilde{E}\alpha\tilde{E}\beta\hat{\omega}e - \lambda\tilde{E}^2\alpha + \hat{E}\alpha\tilde{E}\beta\tilde{\omega}e + \tilde{E}\alpha\tilde{E}\beta\hat{\omega}e \\ &\quad - \lambda\tilde{E}^2\beta + \tilde{E}\alpha\hat{E}\beta\tilde{\omega}e - \hat{E}\alpha\tilde{E}\beta\tilde{\omega}e = -\lambda\left(\tilde{E}^2\alpha + \tilde{E}^2\beta\right) \le 0. \end{aligned} \tag{18}$$

Table 2: Back-EMF fluctuation.

Result	Ea1	Ea2	Unit
Back-EMF fluctuation (a)	7.34~7.32	7.325~7.315	V
Back-EMF fluctuation (b)	22.05~21.925	22.025~22.015	V
Back-EMF fluctuation (c)	80.9 ~ 80.5	80.7 ~ 80.69	V

Therefore, according to the Lyapunov stability criterion, the system with the Kalman filter is stable. The structure schematic diagram of AFG-STA-SMO is shown in Figure 1.

3.4. System Stability Analysis. The Lyapunov function can define as

$$V1 = \frac{1}{2}\left(\tilde{i}\alpha^2 + \tilde{i}\beta^2\right). \tag{19}$$

From equations (19) and (11), it can be obtained that

$$\frac{d}{dt}V1 = -\frac{R}{L}\left(\tilde{i}^2\alpha + \tilde{i}^2\beta\right) - \frac{1}{L}\left(\tilde{e}\alpha\tilde{i}\alpha + \tilde{e}\beta\tilde{i}\beta\right) - k1\left(\left|\tilde{i}\alpha\right|^{3/2} + \left|\tilde{i}\beta\right|^{3/2}\right) < 0. \tag{20}$$

In order to ensure the convergence of the current-sliding mode observer, $(d/dt)V1 < 0$ must satisfy; then, the sliding mode gain $k1$ can be obtained as follows:

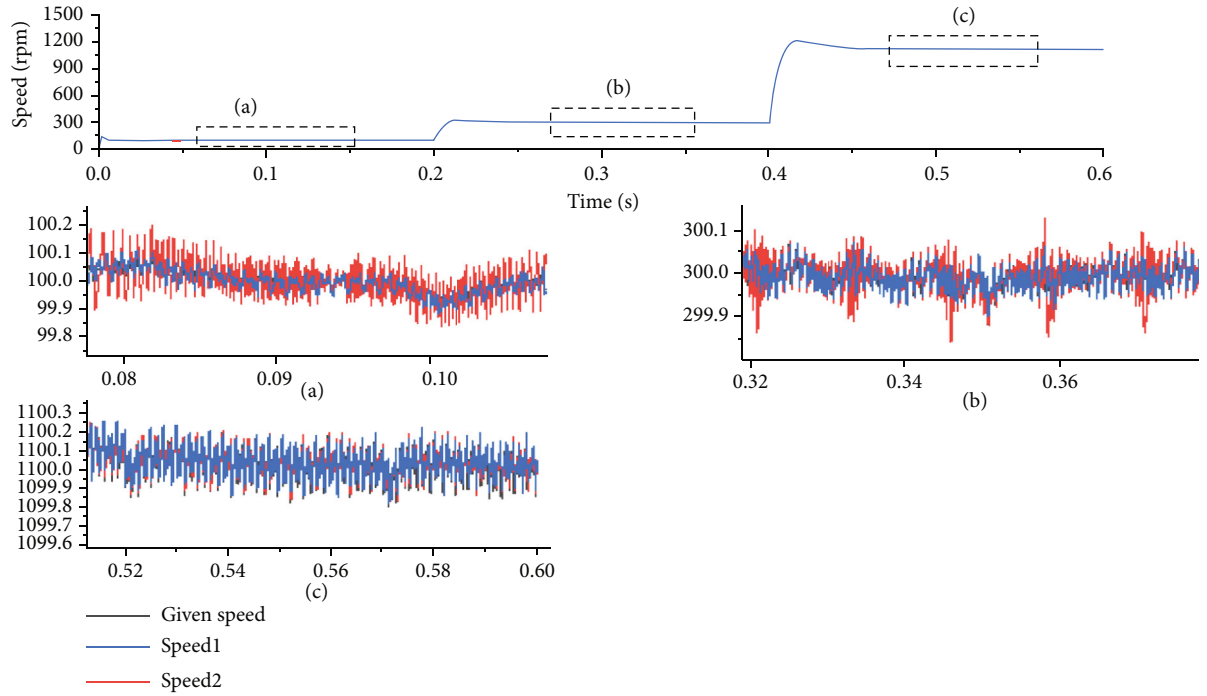

Figure 6: Speed response diagram.

$$k1 > \sup\left\{-\frac{R}{L}\cdot\frac{\left(\tilde{i}^2\alpha+\tilde{i}^2\beta\right)}{\left|\tilde{i}\alpha\right|^{3/2}+\left|\tilde{i}\beta\right|3/2}-\frac{1}{L}\cdot\frac{\tilde{e}\alpha\tilde{i}\alpha+\tilde{e}\beta\tilde{i}\beta}{\left|\tilde{i}\alpha\right|^{3/2}+\left|\tilde{i}\beta\right|^{3/2}}\right\}, \tag{21}$$

where sup {} represents the upper bound.

When the current-sliding mode observer converges, $(d/dt)\tilde{i}\alpha = \tilde{i}\alpha = (d/dt)\tilde{i}\beta = \tilde{i}\beta = 0$, from equation (11) that

$$\begin{cases}\text{sign}\left(\tilde{i}\alpha\right) = -\dfrac{\tilde{e}\alpha}{k1\cdot L\cdot\left|\tilde{i}\alpha\right|^{1/2}},\\ \text{sign}\left(\tilde{i}\beta\right) = -\dfrac{\tilde{e}\beta}{k1\cdot L\cdot\left|\tilde{i}\beta\right|^{1/2}}.\end{cases} \tag{22}$$

Substitute equation (22) into equation (10) and get

$$\begin{cases}\dfrac{d}{dt}\left(v\alpha+lv\alpha\text{eq}\right) = -(1+l)\dfrac{k2\cdot\tilde{e}\alpha}{k1\cdot Ls\cdot\left|\tilde{i}\alpha\right|^{1/2}},\\ \dfrac{d}{dt}\left(v\beta+lv\beta\text{eq}\right) = -(1+l)\dfrac{k2\cdot\tilde{e}\beta}{k1\cdot Ls\cdot\left|\tilde{i}\beta\right|^{1/2}}.\end{cases} \tag{23}$$

It can be obtained from equations (23) and (3) that

$$\begin{cases}\dfrac{d}{dt}\tilde{e}\alpha = -(1+l)\dfrac{k2\cdot\tilde{e}\alpha}{k1\cdot Ls\cdot\left|\tilde{i}\alpha\right|^{1/2}}+\omega e\cdot E\beta,\\ \dfrac{d}{dt}\tilde{e}\beta = -(1+l)\dfrac{k2\cdot\tilde{e}\beta}{k1\cdot Ls\cdot\left|\tilde{i}\beta\right|^{1/2}}-\omega e\cdot E\alpha.\end{cases} \tag{24}$$

Similarly, the Lyapunov function can be defined as

$$V2 = \frac{1}{2}\left(\tilde{e}\alpha^2+\tilde{e}\beta^2\right). \tag{25}$$

From equations (25) and (24), the following equation can be obtained:

$$\begin{aligned}\frac{d}{dt}V2 = &-(1+l)k2\left[\frac{\tilde{e}^2\alpha}{k1\cdot L\cdot\left|\tilde{i}\alpha\right|^{1/2}}+\frac{\tilde{e}^2\beta}{k1\cdot L\cdot\left|\tilde{i}\beta\right|^{1/2}}\right]\\ &+\omega e\cdot E\beta\cdot\tilde{e}\alpha-\omega e\cdot E\alpha\cdot\tilde{e}\beta<0.\end{aligned} \tag{26}$$

To ensure the convergence of the current-sliding mode observer, $(d/dt)V2 < 0$ must satisfy; then, the sliding mode gain $k2$ can be obtained as follows:

$$(1+l)k2 > \sup\left\{\frac{k1\cdot Ls\cdot\omega e\cdot\left(E\beta\cdot\tilde{e}\alpha-E\alpha\cdot\tilde{e}\beta\right)}{\left(\tilde{e}^2\alpha/\left|\tilde{i}\alpha\right|^{1/2}\right)+\left(\tilde{e}^2\beta/\left|\tilde{i}\beta\right|^{1/2}\right)}\right\}. \tag{27}$$

Equations (21) and (27) give the stability conditions of the established system.

3.5. Adaptive Law Analysis of Feedback Gain Coefficient. In equation (20), $-R/L(\tilde{i}^2\alpha+\tilde{i}^2\beta)$ and $-k1(\left|\tilde{i}\alpha\right|^{3/2}+\left|\tilde{i}\beta\right|^{3/2})$ is always less than 0. A sufficient condition for the existence of equation (20) is constructed as follows:

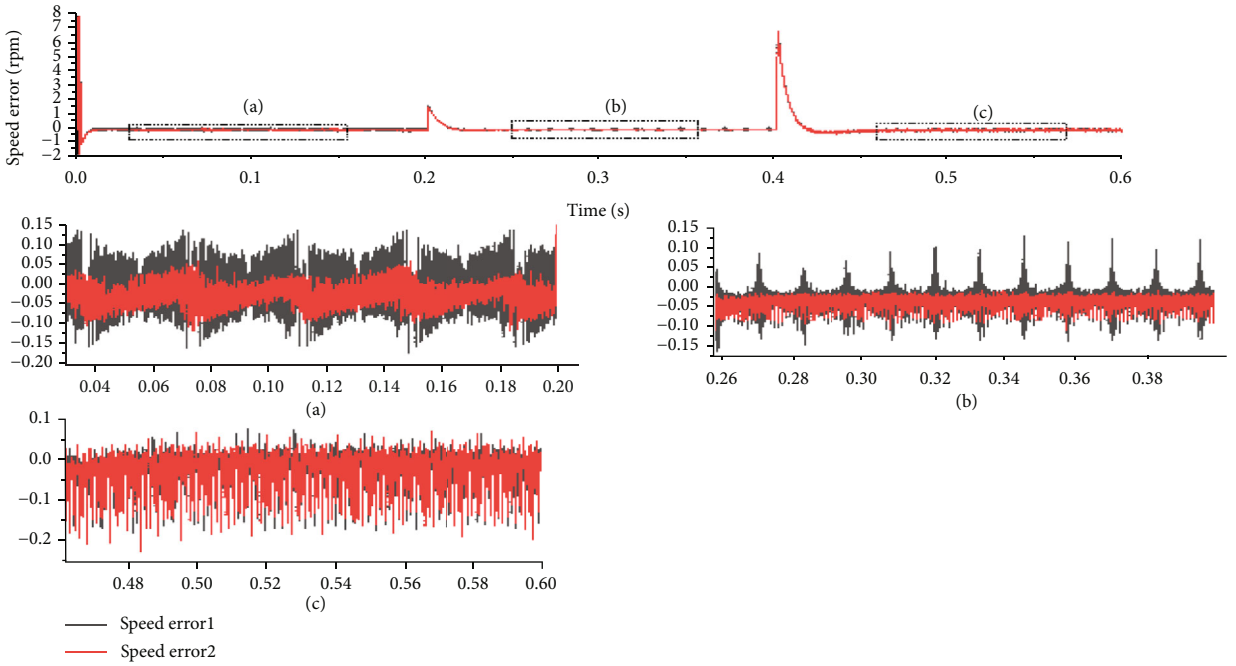

Figure 7: Speed error response diagram.

$$\begin{cases} -\frac{R}{L}\left(\tilde{i}^2\alpha + \tilde{i}^2\beta\right) - \frac{1}{L}\left(\tilde{e}\alpha\tilde{i}\alpha + \tilde{e}\beta\tilde{i}\beta\right) - k1\left(\left|\tilde{i}\alpha\right|^{3/2} + \left|\tilde{i}\beta\right|^{3/2}\right) < 0, & \tilde{i}\alpha > 0, \tilde{i}\beta > 0, \\ -\frac{R}{L}\left(\tilde{i}^2\alpha + \tilde{i}^2\beta\right) - \frac{1}{L}\left(-\tilde{e}\alpha\tilde{i}\alpha - \tilde{e}\beta\tilde{i}\beta\right) - k1\left(\left|\tilde{i}\alpha\right|^{3/2} + \left|\tilde{i}\beta\right|^{3/2}\right) < 0, & \tilde{i}\alpha < 0, \tilde{i}\beta < 0. \end{cases} \tag{28}$$

Since $-R/L(\tilde{i}^2\alpha + \tilde{i}^2\beta) < 0$ and $-k1(|\tilde{i}\alpha|^{3/2} + |\tilde{i}\beta|^{3/2}) < 0$, it can be deduced that the condition satisfying $(d/dt)V1 < 0$ is as follows:

$$(1 + l)k2 > \max\left(|E\alpha|, |E\beta|\right) = |\omega e|\psi f, \tag{29}$$

where ωe is the actual speed and ψf is the flux linkage.

From equation (29), it can be seen that the selection of l affects the size of the sliding mode gain of $k2$. The larger the l is, the lower the limit of the effective range of $k2$ is. Conversely, the smaller the l is, the higher the lower limit of the effective range of $k2$ is.

According to equation (29),

$$l > \frac{|\omega e|\psi f}{k2} - 1, \tag{30}$$

where $k2 > \psi f$.

According to equation (30), $1 > (\psi f/k2) > 0$ is known, so the feedback gain coefficient l can be designed as follows:

$$l = \delta|\omega e| - 1, \tag{31}$$

where δ is a normal number, which is related to the gain of sliding mode $k2$. So $k2$ meet the following conditions:

$$k2 > \frac{\psi f}{\delta}. \tag{32}$$

Table 3: Back-EMF fluctuation.

Result	FFG-STA-SMO	AFG-STA-SMO	Unit
Error (a)	0.3225	0.175	Rpm
Error (b)	0.275	0.0975	Rpm
Error (c)	0.27	0.27	Rpm
Position error (a)	0.0043	0.0007	Deg
Position error (b)	0.00037	0.00009	Deg
Position error (c)	0.00016	0.00016	Deg

In order to select δ conveniently, $0 < \delta < 1$ is set in this paper.

4. Rotor Position Estimation

Since the sliding mode control is accompanied by high-frequency chattering in the sliding mode, the high-frequency chattering phenomenon will estimate in the back-EMF. The rotor position estimation method based on the arctangent function will introduce this chattering into the division operation; significantly, when the observed value of back-EMF exceeds zero, the rotor error will amplify. Therefore, PLL [25] is adopted in this paper to replace the arctangent function to extract the rotor's position information, as shown in Figure 2.

Hypothesis $\eta = (Ld - Lq)(\omega eid - piq) + \hat{\omega}e\zeta f$, when $|\theta e - \hat{\theta}e| < \pi/6$ and $\sin(\theta e - \hat{\theta}e) = (\theta e - \hat{\theta}e)$ is established, according to Figure 2, can get the following relationship:

$$\begin{aligned} \Delta E &= -\hat{E}\alpha\cos\hat{\theta}e - \hat{E}\beta\sin\hat{\theta}e = \eta\sin\theta e\cos\hat{\theta}e - \eta\sin\hat{\theta}e\cos\theta e \\ &= \eta\sin\left(\theta e - \hat{\theta}e\right) \approx \eta\left(\theta e - \hat{\theta}e\right). \end{aligned} \tag{33}$$

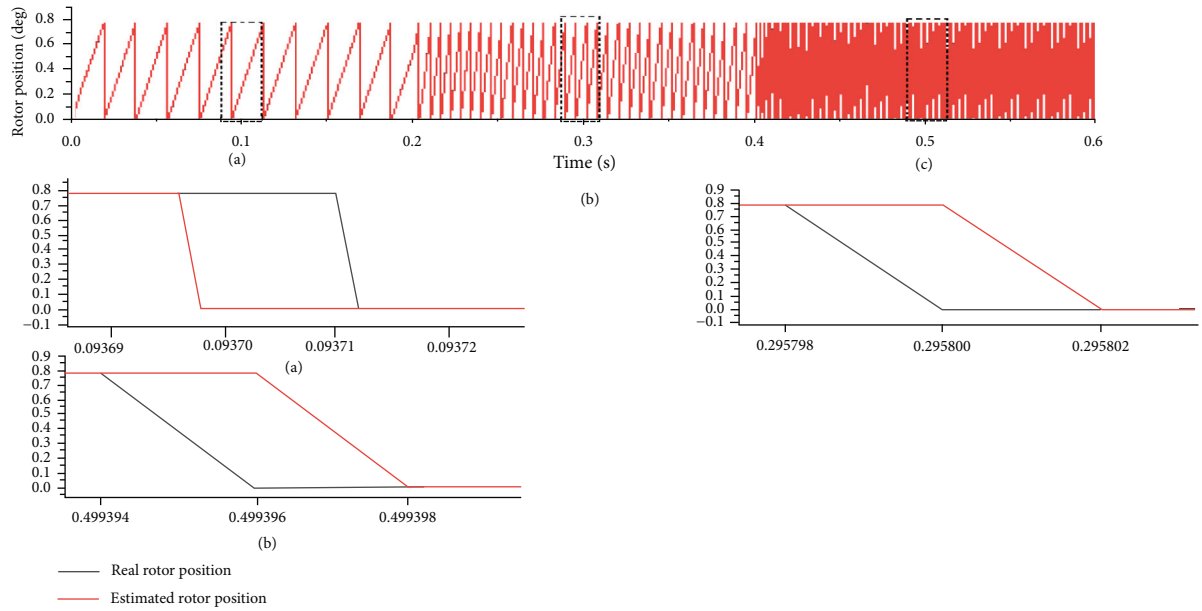

Figure 8: Rotor position change with fixed feedback gain.

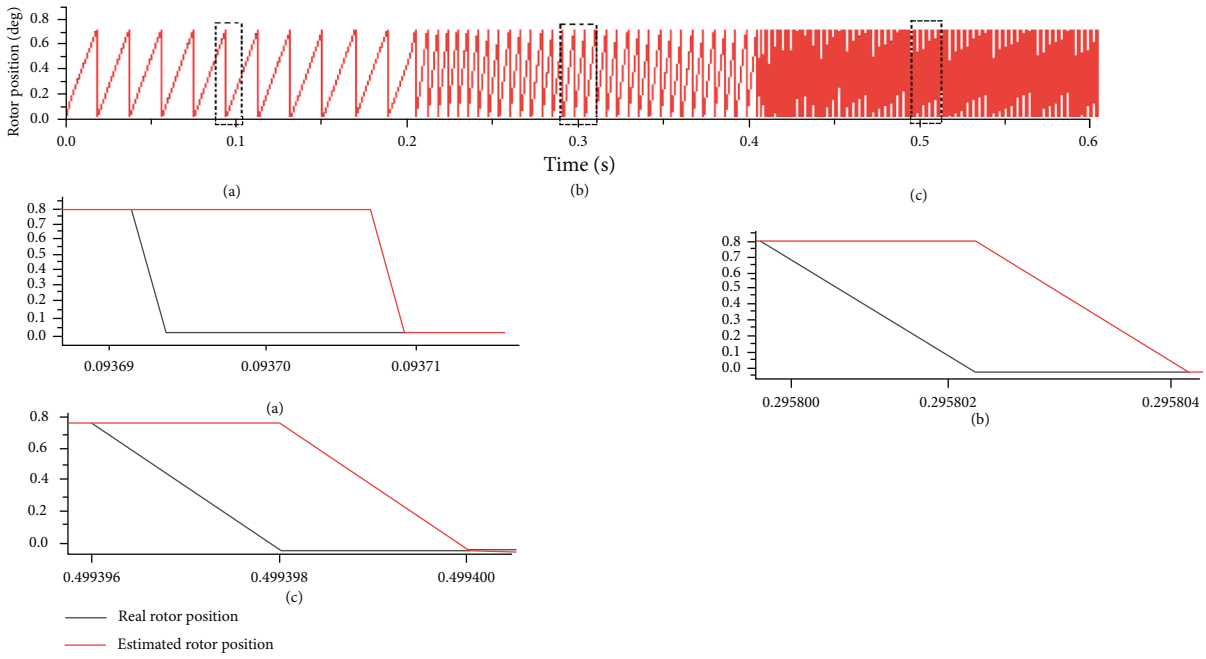

Figure 9: Rotor position change with adaptive feedback gain.

At this time, the equivalent block diagram of Figure 2 is shown in Figure 3.

According to Figure 3, the transfer function of PLL can be obtained, namely,

$$G(s) = \frac{\widehat{\theta}e}{\theta e} = \frac{2\xi\omega n + \omega^2 n}{s^2 + 2\xi\omega n s + \omega^2 n}, \tag{34}$$

where $\omega n = (Kp/2)\sqrt{\eta/Ki}$, $\xi = \sqrt{\eta Ki}$, and ωn determine the bandwidth of the PI regulator.

5. Simulation

According to Figure 4, MATLAB is used to build a simulation model, and the control scheme adopts vector control based on id = 0. The motor parameters in the simulation experiment are shown in Table 1.

The control system parameters of SPMSM based on the traditional sliding mode observer are as follows: $k = 200$. The control system parameters of SPMSM based on traditional STA-SMO are as follows: $k_1 = 5000$ and $k_2 = 200000$. The control system parameters of STA-SMO PMSM based on

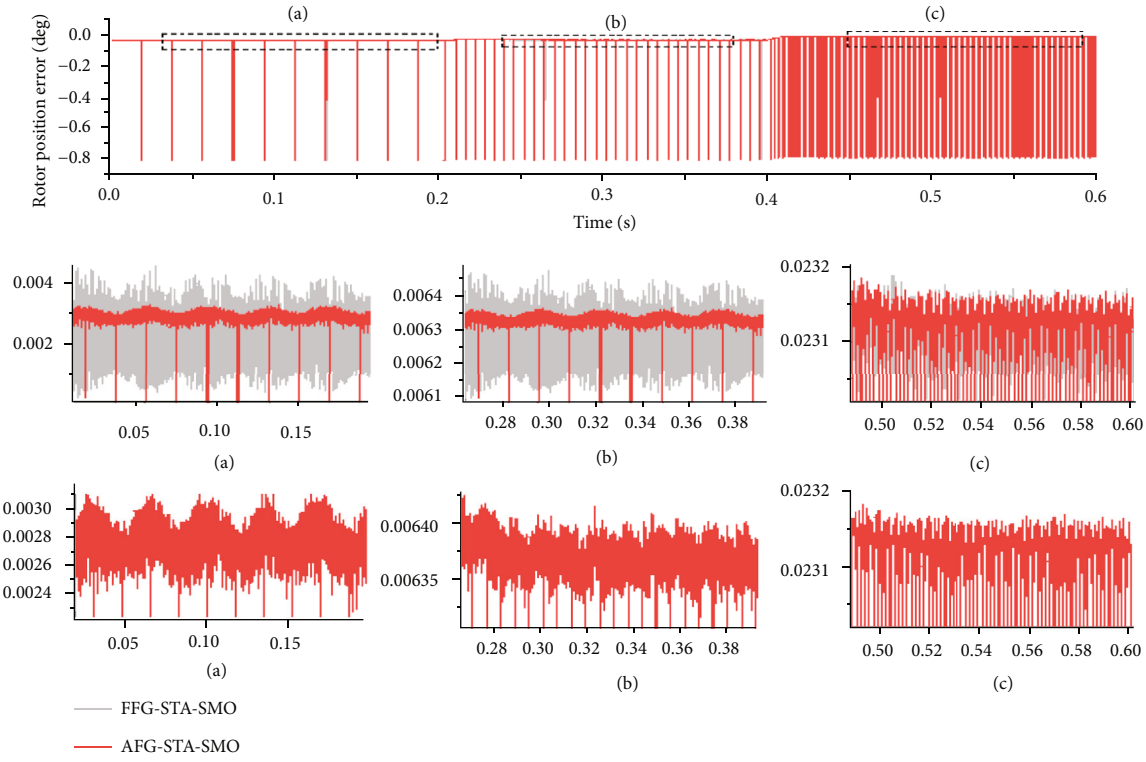

Figure 10: Rotor position error diagram.

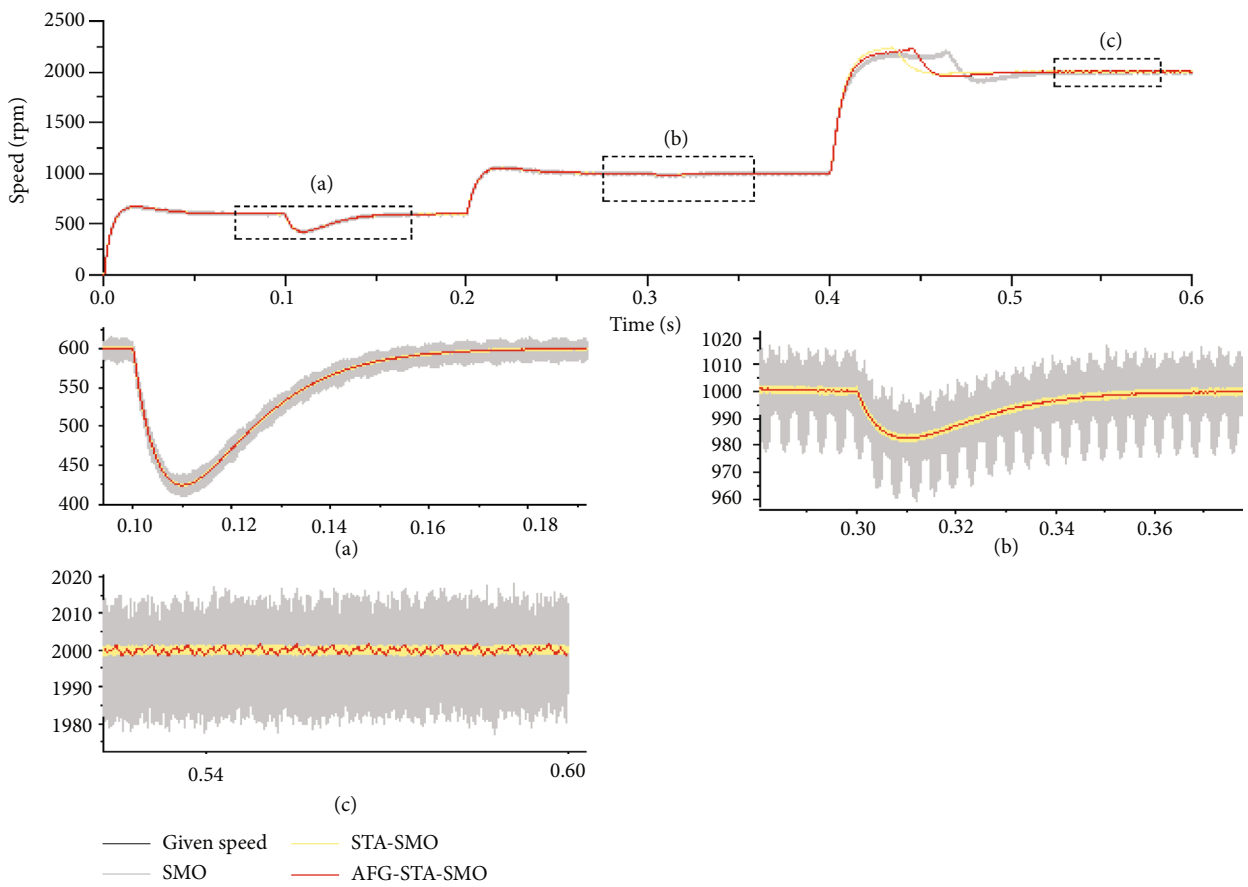

Figure 11: Speed response diagram.

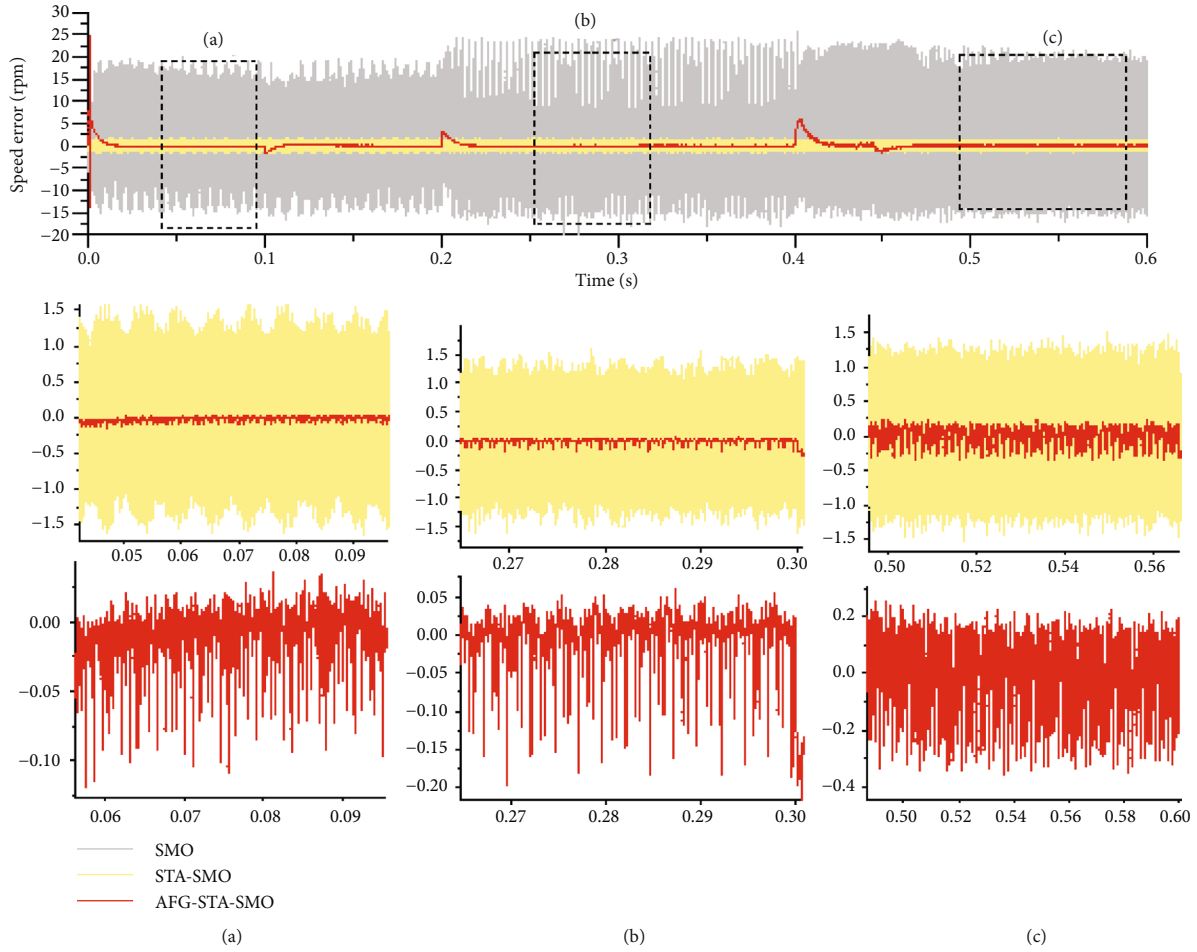

Figure 12: Speed error response diagram.

fixed feedback gain are $k_1 = 5000$, $k_2 = 700$, and $l = 500$. The control system parameters of PMSM based on AFG-STA-SMO are as follows: $k_1 = 5000$, $k_2 = 700$, and $\delta = 0.5$.

5.1. Improved AFG-STA-SMO Simulation. When the SPMSM is under sensor-less control, the rotor position and speed signals are hidden in the back-EMF observation value. This paper mainly uses a super spiral sliding mode observer to extract rotor position and speed information from the back-EMF observations. Although this strategy can avoid introducing low-pass filters, it cannot effectively filter the back-EMF ripple component. In order to obtain a smooth back-EMF signal, this article introduces a Kalman filter to filter the back-EMF signal again. The simulation result is shown in Figure 5. To verify the effectiveness of the strategy proposed in this paper, the motor adopts a no-load starting mode with a given speed of 100 r/min. At 0.2 s, the speed is increased to 300 r/min; at 0.4 s, the speed is increased to 1100 r/min. Figure 5 shows the back-EMF response waveforms under two different strategies.

Table 2 shows that the back-EMF fluctuations of the improved strategy proposed in this paper at three different speed stages are 50%, 8%, and 2.5% of the back-EMF fluctuations of the unimproved strategy, respectively.(Ea1: AFG-STA-SMO without Kalman filter; Ea2: AFG-STA-SMO with Kalman filter). By analyzing Figure 5 and the above results, it can be seen that the introduction of the Kalman filter can effectively suppress the ripple component in the back-EMF observation value, thereby obtaining a smoother back-EMF observation signal and further improving the accuracy of the rotor position estimation.

Table 4: Speed Error.

Result	SMO	STA-SMO	AFG-STA-SMO	Unit
Error (a)	35	3	0.15	Rpm
Error (b)	45	3	0.25	Rpm
Error (c)	40	3	0.6	Rpm

5.2. Verification of Adaptive Feedback Gain Adjustment. In order to verify the validity of the adaptive law proposed in this article, the motor adopts a no-load starting mode with a given speed of 100 r/min. At 0.2 s, the speed is increased to 300 r/min; at 0.4 s, the speed is increased to 1100 r/min.

From Figures 6 and 7 and Table 3, it is shown that the speed errors of AFG-STA-SMO at three different speed stages are 54.26%, 35.45%, and 100% of STA-SMO speed errors with fixed feedback gain (FFG-STA-SMO), respectively.

Table 5: THD and back-EMF fluctuation.

Result	SMO	STA-SMO	AFG-STA-SMO	Unit
THD (a)	8.92	8.62	8.68	%
THD (b)	1.84	1.27	1.24	%
THD (c)	1.50	4.28	3.84	%
Back-EMF fluctuation (a)	-31.8~-33.725	-32.92~-33	-32.91~-32.92	V
Back-EMF fluctuation (b)	-72~-72.36	-72.6~-72.76	-72.685~-72.695	V
Back-EMF fluctuation (c)	143~145	146.35~146.6	46.22~146.23	V

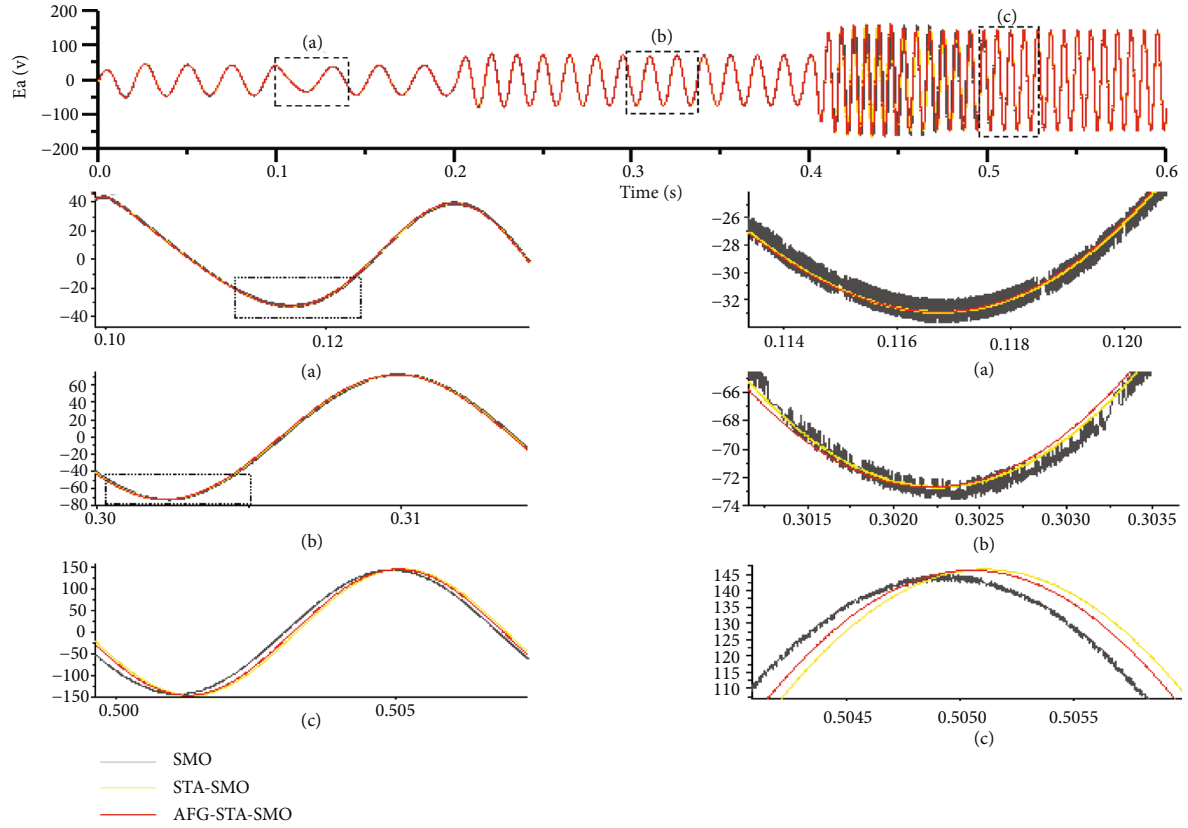

Figure 13: Response diagram of back-EMF.

Figures 8–10 and Table 3 show that the rotor position errors of AFG-STA-SMO at three different speed stages are 16.28%, 24.32%, and 100% of FFG-STA-SMO rotor position errors, respectively.

From the above results and the simulation diagram analysis, it can be seen that under the action of the fixed feedback gain, when the motor is running at 1000 r/min, the speed error and rotor position error are minimal. As the speed continues to decrease, the speed error and rotor position error are gradually increasing. After introducing adaptive control, the feedback gain is proportional to the speed. During the entire speed change process, the speed errors are less than the speed errors of FFG-STA-SMO; the estimated rotor position and the actual rotor position are the same, enhancing the system stability.

5.3. Medium and High-Speed Verification Analysis. In order to verify the advantages of the control strategy proposed in this paper in medium and high-speed operation, the motor adopts a no-load starting mode, and the given speed is 600 r/min. At 0.1 s, load torque of 4.5 N·m is applied; at 0.2 s, the speed rises to 1000 r/min; at the first variable speed stable operation stage (0.3 s), the load torque changes to 5 N·m; at 0.4 s, the speed is increased to 2000 r/min.

From Figure 11, the application of 4.5 N·m and 5 N·m of load torque in 0.1 s and 0.3 s, respectively, causes a slight speed drop in the actual speed. At this time, the estimated speed is still tracking the actual speed, and there is also a slight speed drop that has proved the feasibility and effectiveness of these three control strategies.

Figure 12 and Table 4 show that the speed errors of AFG-STA-SMO at three different speed stages are 0.429%, 0.556%, and 1.5% of SMO speed errors, respectively. The speed errors of AFG-STA-SMO at three different speed stages are 5%, 8.3%, and 20% of STA-SMO speed errors, respectively.

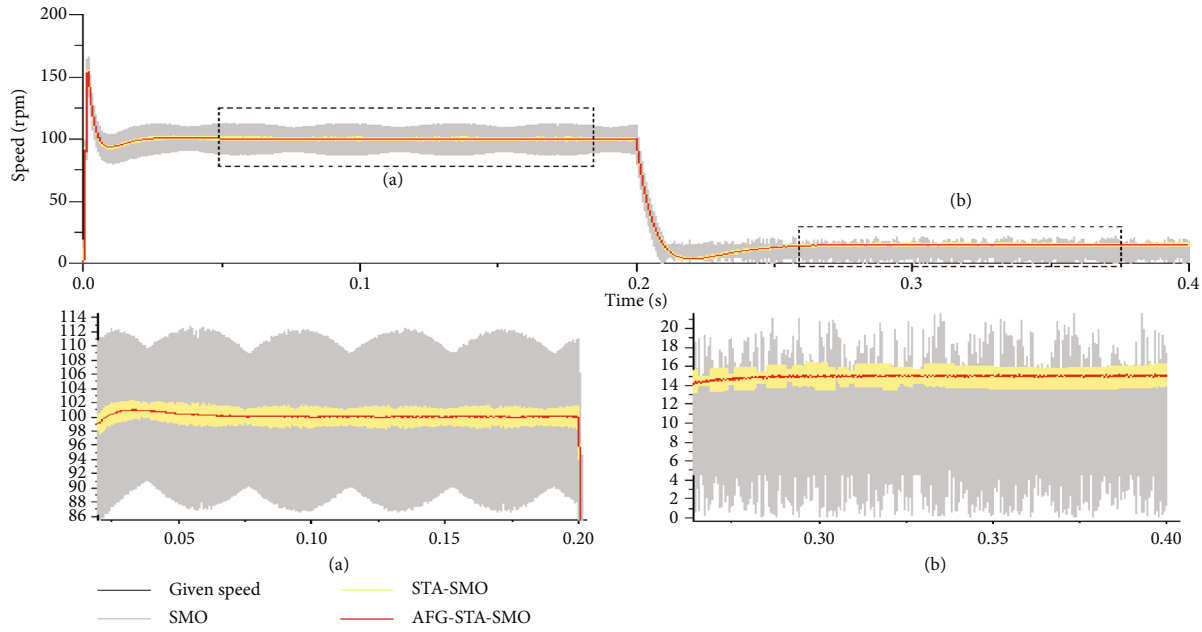

Figure 14: Response diagram of speed.

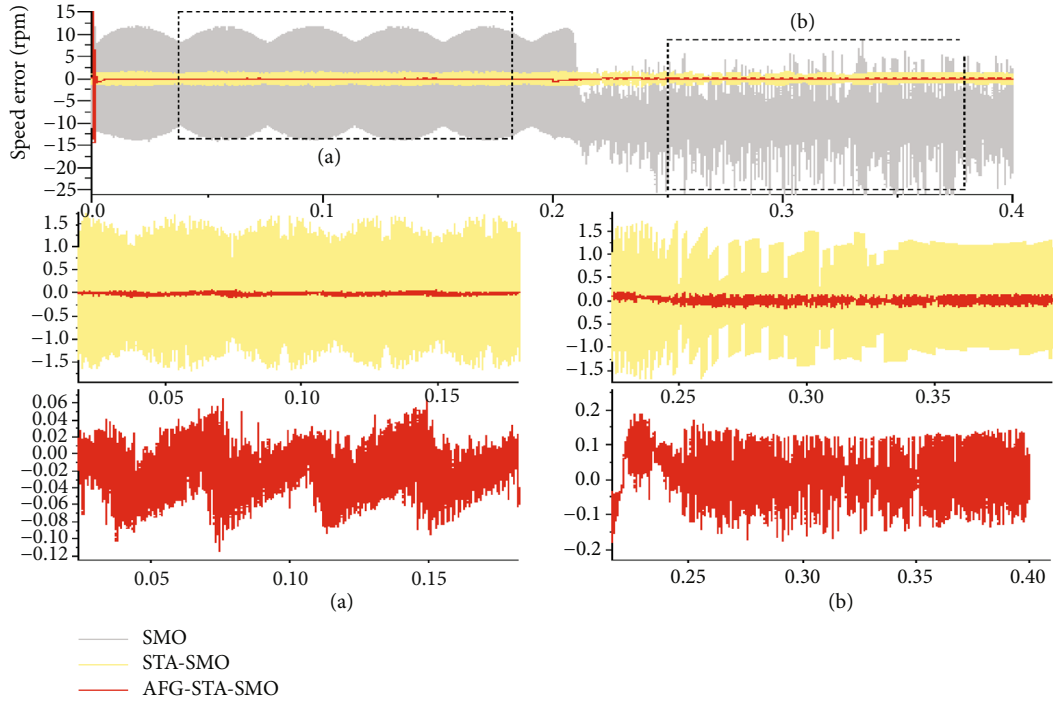

Figure 15: Response diagram of speed error.

From the above results and simulation waveform analysis, it can be seen that the speed error of SMO increases with the continuous increase of the speed; the sliding mode chattering is serious, which is not conducive to the system's stable operation of the system. There is an obvious lag phenomenon in the speed rise of 2000 r/min. Compared with SMO, STA-SMO effectively suppresses sliding mode chattering due to the characteristics of high-order sliding

Table 6: Speed error and rotor position error.

Result	SMO	STA-SMO	AFG-STA-SMO	Unit
Error (a)	26	3.2	0.17	Rpm
Error (b)	35	3.2	0.4	Rpm
Position error (a)	0.3	0.03	0.0016	Deg
Position error (b)	0.8	0.2	0.006	Deg

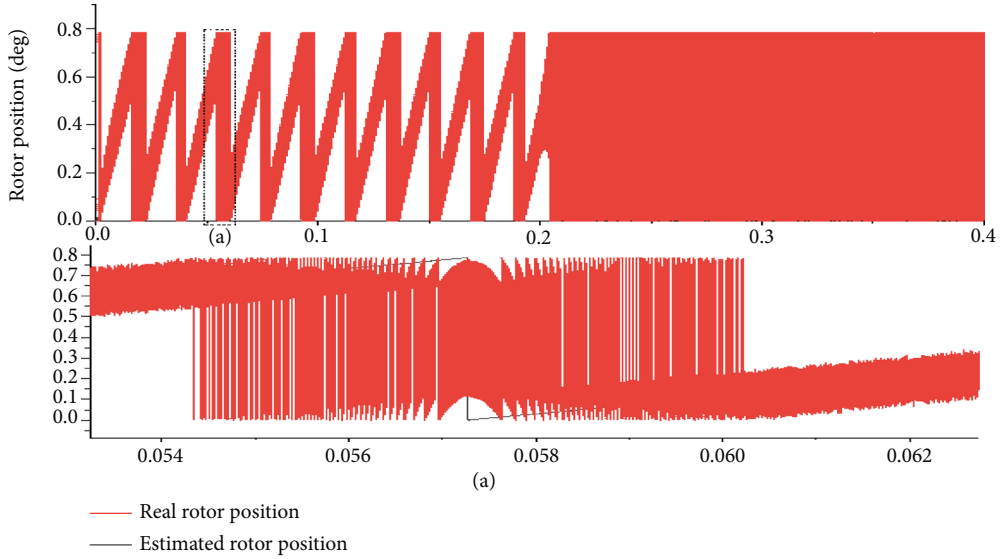

Figure 16: The rotor position change of traditional SMO.

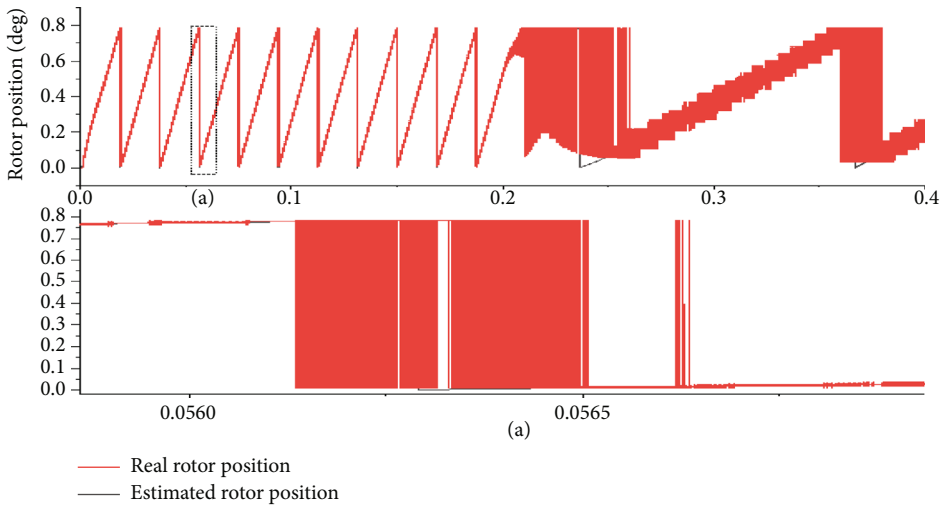

Figure 17: The rotor position change of traditional STA-SMO.

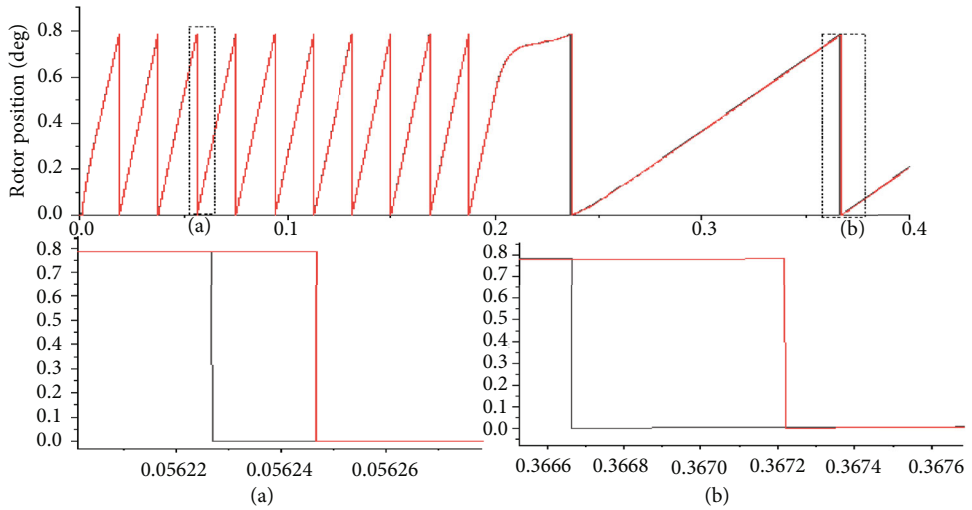

Figure 18: The rotor position change of AFG-STA-SMO.

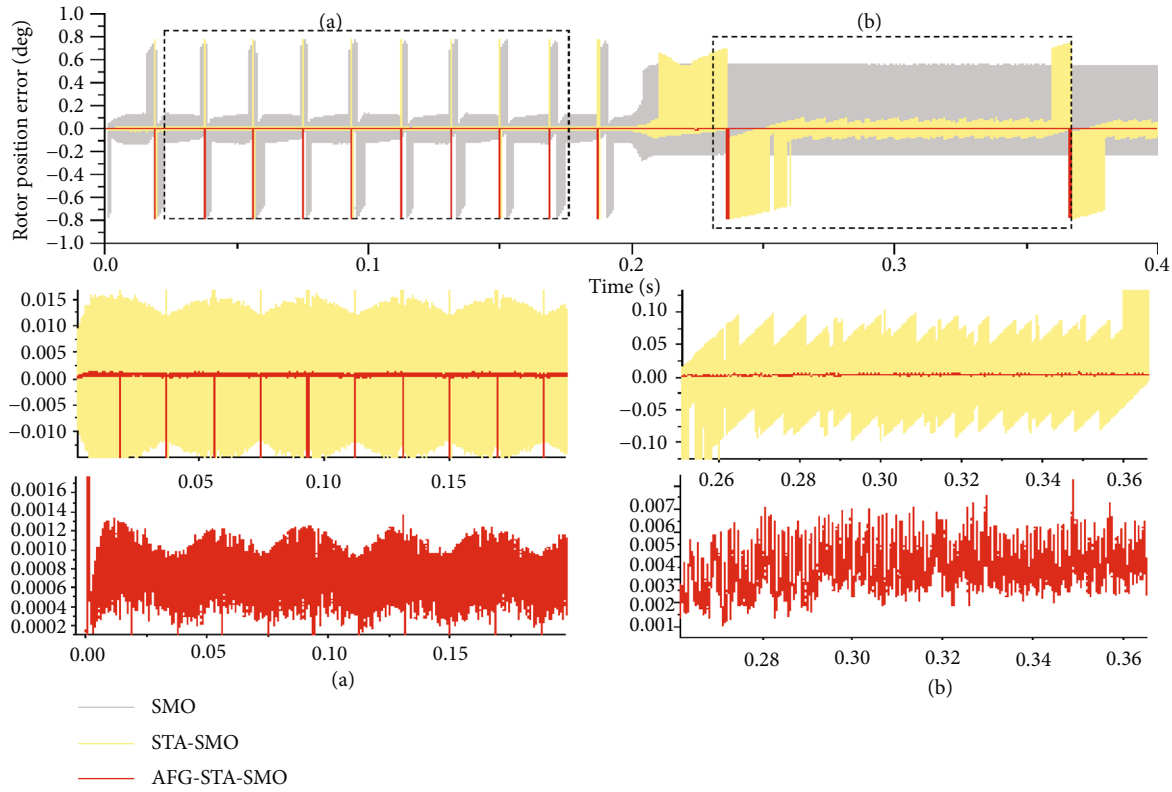

Figure 19: Rotor position error of the response diagram.

mode and integral operation function and reduces the speed error, thereby avoiding the lag phenomenon caused by introducing low-pass filters. Compared with STA-SMO, the proposed control strategy is based on STA-SMO, and the Kalman filter and adaptive control are introduced to suppress further sliding mode chattering so that the speed error is minimized, and the change of speed error is small when coping with external disturbance.

Table 5 shows that the back-EMF fluctuations of AFG-STA-SMO at three different speed stages are 0.75%, 2.78%, and 0.5% of the back-EMF fluctuations of SMO, respectively. The back-EMF fluctuations of AFG-STA-SMO at three different speed stages are 12.5%, 6.25%, and 4% of the back-EMF fluctuations of STA-SMO, respectively.

Figure 13, Table 5, and the above analysis of the results show that the SMO's back-EMF has a lag due to the low-pass filter's introduction, which affects the system's response speed. However, STA-SMO avoids this phenomenon due to integral operation. Although these two control strategies can effectively filter out the harmonic components, there are many ripple components in the back-EMF value. If they are directly used to estimate the rotor position, they will inevitably cause larger errors. Therefore, the Kalman filter is introduced to perform filtering processing to effectively suppress the back-EMF ripple component, thereby obtaining a smoother back-EMF signal and improving control accuracy.

5.4. Low-Speed Verification Analysis. In order to verify the advantages of the sensor-less algorithm-controlled speed control system in low-speed operation situations, simulation experiments are carried out in low-speed areas. The motor adopts a no-load start mode, and the given speed is 100 r/min. At 0.2 s, the speed suddenly changes to 15 r/min.

Figure 14, Figure 15, and Table 6 show that the speed errors of AFG-STA-SMO at two different speed stages are 0.6534% and 1.1423% of the SMO speed errors, respectively. The speed errors of AFG-STA-SMO at two different speed stages are 5.3125% and 12.5% of STA-SMO speed errors, respectively.

Figures 16–19 and Table 6 show that the rotor position errors of AFG-STA-SMO at two different speed stages are 0.53% and 0.75% of SMO rotor position errors, respectively. The rotor position errors of AFG-STA-SMO at two different speed stages are 5.33% and 3% of STA-SMO rotor position errors, respectively.

From the above results and simulation diagram analysis, it can be seen that when the motor runs at low speed, the chattering of SMO speed waveform and rotor estimated position waveform is serious, and the speed error and rotor position error are the largest. When the speed is reduced to 15 r/min, the system almost cannot operate normally. Compared with SMO, STA-SMO suppresses sliding mode chattering to a certain extent due to the characteristics of high-order sliding mode and the function of the integrator. However, the back-EMF is too small when the motor runs at low speed, resulting in rotor position error and speed error deviation. It is not conducive to the stable operation of the system. Compared with STA-SMO, the estimated rotor position of AFG-STA-SMO is basically the same as the actual rotor position due to the introduction of

equivalent feedback gain, and the speed error and rotor position error are minimal, thus avoiding the situation that the rotor position error is too large due to the small back-EMF.

6. Conclusion

This paper presents a sensor-less control strategy for STA-SMO with adaptive feedback gain. The adaptive law, which compensates for rotor angle estimation error by adjusting the feedback gain coefficient online, effectively solves the motor's problems of low-speed operation difficulty and serious sliding mode chattering.

Secondly, the Kalman filter is used to reduce the ripple component in the back-EMF. The smoother back-EMF signal is obtained, and the control precision of the algorithm is further improved.

The whole system realizes the full speed domain operation; the dynamic response is fast and has the strong disturbance resistance when dealing with the external disturbance. In the next step, the author intends to implement the proposed control strategy with high-performance DSP chip in order to improve the operation time extension caused by the increasing complexity of the control system.

Data Availability

The data supporting the findings of this study are available within the article.

Conflicts of Interest

The authors declare that they have no conflicts of interest.

Acknowledgments

This research work was supported by the Jilin Science and Technology Development Project 20200403133SF.

References

[1] L. Zhang, S. Wang, and J. Bai, "Fast-super-twisting sliding mode speed loop control of permanent magnet synchronous motor based on SVM-DTC," *IEICE Electronics Express*, vol. 18, no. 1, article 20200375, 2021.

[2] B. K. Bose, "Power electronics and motion control-technology status and recent trends," *IEEE Transactions on Industry Applications*, vol. 29, no. 5, pp. 902–909, 1993.

[3] F. Dongxue, X. Zhao, and H. Yuan, "High-precision motion control method for permanent magnet linear synchronous motor," *IEICE Electronics Express*, vol. 18, article 20210097, 2021.

[4] X. Zhao and D. Fu, "Adaptive neural network nonsingular fast terminal sliding mode control for permanent magnet linear synchronous motor," *IEEE Access*, vol. 7, pp. 180361–180372, 2019.

[5] T. M. Jahns and V. Blasko, "Recent advances in power electronics technology for industrial and traction machine drives," *Proceedings of the IEEE*, vol. 89, no. 6, pp. 963–975, 2001.

[6] G. Foo and M. F. Rahman, "Sensorless sliding-mode MTPA control of an IPM synchronous motor drive using a sliding-mode observer and HF signal injection," *IEEE Transactions on Industrial Electronics*, vol. 57, no. 4, pp. 1270–1278, 2010.

[7] L. Ding, Y. W. Li, and N. R. Zargari, "Discrete-time SMO sensorless control of current source converter-fed PMSM drives with low switching frequency," *IEEE Transactions on Industrial Electronics*, vol. 68, no. 3, pp. 2120–2129, 2021.

[8] Q. Zhu, Z. Li, and X. Tan, "Sensors fault diagnosis and active fault-tolerant control for PMSM drive systems based on a composite sliding mode observer," *Energies*, vol. 12, no. 9, p. 1695, 2019.

[9] W. Zhu, "A position sensorless control strategy for SPMSM based on an improved sliding mode observer," *IOP Conference Series Earth and Environmental Science*, vol. 252, article 032135, 2019.

[10] K. Prabhakaran, K. Anbalagan, and F. Blaabjerg, "Laboratory implementation of electromagnetic torque based MRAS speed estimator for sensorless SMPMSM drive," *Electronics Letters*, vol. 55, no. 21, pp. 1145–1147, 2019.

[11] E. Dehghan-Azad, S. Gadoue, D. Atkinson, H. Slater, P. Barrass, and F. Blaabjerg, "Sensorless control of IM based on stator-voltage MRAS for limp-home EV applications," *IEEE Transactions on Power Electronics*, vol. 33, no. 3, pp. 1911–1921, 2018.

[12] Z. Yin, G. Li, Y. Zhang, and J. Liu, "Symmetric-strong-tracking-extended-Kalman-filter-based sensorless control of induction motor drives for modeling error reduction," *IEEE Transactions on Industrial Informatics*, vol. 15, no. 2, pp. 650–662, 2019.

[13] J. Sun, G. Cao, S. Huang, Y. Peng, J. He, and Q. Qian, "Sliding-mode-observer-based position estimation for sensorless control of the planar switched reluctance motor," *IEEE Access*, vol. 7, pp. 61034–61045, 2019.

[14] C. M. Verrelli, S. Bifaretti, E. Carfagna et al., "Speed sensor fault tolerant PMSM machines: from position-sensorless to sensorless control," *IEEE Transactions on Industry Applications*, vol. 55, no. 4, pp. 3946–3954, 2019.

[15] K. Paponpen and M. Konghirun, "An improved sliding mode observer for speed sensorless vector control drive of PMSM," in *2006 CES/IEEE 5th international power electronics and motion control conference*, pp. 1–5, Shanghai, 2006.

[16] L. Guo, X. Zhang, S. Yang, Z. Xie, L. Qi, and L. Wang, "Super-twisting sliding mode observer based speed sensorless torque control for PMSG used in wind turbines," in *2015 9th International Conference on Power Electronics and ECCE Asia (ICPE-ECCE Asia)*, pp. 2457–2462, Seoul, 2015.

[17] A. Levant, "Principles of 2-sliding mode design," *Automatica*, vol. 43, no. 4, pp. 576–586, 2007.

[18] D. Wang, J. Liu, S. Miao et al., "Rotor position estimation method for permanent magnet synchronous motor based on super-twisting sliding mode observer," in *2018 37th Chinese Control Conference (CCC)*, pp. 5634–5638, Wuhan, 2018.

[19] S. Chi, Z. Zhang, and L. Xu, "Sliding-mode sensorless control of direct-drive PM synchronous motors for washing machine applications," *IEEE Transactions on Industry Applications*, vol. 45, no. 2, pp. 582–590, 2009.

[20] S. Chi, L. Xu, and Z. Zhang, "Sliding mode sensorless control of PM synchronous motor for direct-driven washing machines," in *Conference Record of the 2006 IEEE industry applications conference forty-first IAS annual meeting*, pp. 873–879, Tampa, FL, 2006.

[21] S. Chi, Z. Zhang, and L. Xu, "A novel sliding mode observer with adaptive feedback gain for PMSM sensorless vector control," in *2007 IEEE power electronics specialists conference*, pp. 2579–2585, Orlando, FL, 2007.

[22] F. Zhao, L. U. O. Wen, G. A. O. Fengyang, and Y. U. Jiale, "Based on the fuzzy sliding mode control and two stage filtering all-digital fuzzy sliding mode observer is improved control strategy (English)," *Journal of Measurement Science and Instrumentation*, vol. 1, no. 11, 2020.

[23] Y. Fan, L. Zhang, M. Cheng, and K. T. Chau, "Sensorless SVPWM-FADTC of a new flux-modulated permanent-magnet wheel motor based on a wide-speed sliding mode observer," *IEEE Transactions on Industrial Electronics*, vol. 62, no. 5, pp. 3143–3151, 2015.

[24] C. Junjie, *Sensorless Control of Permanent Magnet Synchronous Motor Based on Improved Sliding Mode Observer*, Shanghai Institute of Electrical Engineering, 2019.

[25] G. Wang, Z. Li, G. Zhang, Y. Yu, and D. Xu, "Quadrature PLL-based high-order sliding-mode observer for IPMSM sensorless control with online MTPA control strategy," *IEEE Transactions on Energy Conversion*, vol. 28, no. 1, pp. 214–224, 2013.